Electronic Supplementary Material (ESI) for RSC Advances.


# Supplementary Information

## Large-scale synthesis of mixed valance $K_3[Fe_2S_4]$ with high dielectric and ferrimagnetic characteristics

Mohammad R. Ghazanfari [a], Archa Santhosh [b], Johannes C. Vrijmoed [c], Konrad Siemensmeyer [d], Bertram Peters [e], Stefanie Dehnen [e], Paul Jerabek [b], Günther Thiele *[a]

a: Fachbereich Biologie, Chemie, Pharmazie, Freie Universität Berlin, Fabeckstr. 34-36, 14195 Berlin, Germany
b: Institute of Hydrogen Technology, Helmholtz-Zentrum Hereon, Max-Planck Straße 1, 21502 Geesthacht, Germany
c: Fachbereich Geowissenschaften, Freie Universität Berlin, Malteserstr. 74-100, 12249 Berlin, Germany
d: Helmholtz-Zentrum Berlin für Materialien und Energie, Hahn-Meitner-Platz 1, 14109 Berlin, Germany
e: Fachbereich Chemie, Philips-Universität Marburg, Hans-Meerwein-Straße 4, 35032 Marburg, Germany

*Corresponding author: Dr. Günther Thiele; E-mail: guenther.thiele@fu-berlin.de

**Contents**



## 1. Details of single crystal XRD measurement and refinement

Single crystals were mounted in Paratone® crystallographic oil according to the reported procedure,[S1] and measured using a *Bruker D8 Venture* diffractometer with a *Photon 100 CMOS* area detector at 100 K with Mo-$K_\alpha$ radiation ($\lambda$ = 0.71 Å). Using *Olex2*[S2] the solid-state structure was solved by *ShelXT*[S3] and refined using the *ShelXL* software.[S4] Figures of the structure were depicted with *DIAMOND 4.5.2*.[S5]

*Crystal data:* **1** (186.99 g·mol$^{-1}$) crystallises in the orthorhombic space group: *Pnma*, $a$ = 7.1219(4) Å, $b$ = 10.9301(6) Å, $c$ = 11.4840(7) Å, $V$ = 893.95(9) Å$^3$., $T$ = 100(2) K, $\rho_{calc}$ = 2.654 g·cm$^{-1}$, $\mu$(*Mo* $K_\alpha$) = 5.485 mm$^{-1}$, *GooF* = 1.141, $R_{int}$ = 0.0896, Crystal Dimensions (mm$^3$) = 0.152 × 0.0.097 × 0.0.094, 19979 reflections collected (5.146° < $2\Theta$ < 61.65°) Multi-scan absorption correction was applied with *SADABS*.[S6] The final refinement values were $R_1$ = 0.0428 ($I > 2\,\sigma(I)$), and $wR_2$ = 0.0724 (all data).

Full data of the refinement details are provided in tables S1 to S3.

**Table S1.** Fractional atomic coordinates (×$10^4$) and equivalent isotropic displacement parameters (Å$^2$×$10^3$) for compound **1**. $U_{eq}$ is defined as $\frac{1}{3}$ of the trace of the orthogonalised $U_{IJ}$ tensor

| Atom | *x* | *y* | *z* | $U_{eq}$ |
|---|---|---|---|---|
| Fe1 | 4484.6(7) | 6230.1(5) | 5317.9(5) | 5.91(12) |
| K2 | –825.5(16) | 7500 | 2690.2(10) | 7.7(2) |
| K3 | 9378.5(11) | 9247.4(7) | 6382.8(7) | 10.07(16) |
| S4 | 5957.0(18) | 7500 | 6597.2(12) | 7.2(2) |
| S5 | 2103.1(17) | 7500 | 4672.6(12) | 7.2(2) |
| S6 | 3444.7(13) | 4442.0(8) | 6129.5(8) | 7.25(17) |

**Table S2.** Anisotropic displacement parameters (Å$^2$×$10^3$) for compound **1**. The anisotropic displacement factor exponent takes the form: $-2\pi^2[h^2a\cdot 2U_{11}+2hka\cdot b\cdot U_{12}+\ldots]$

| Atom | $U_{11}$ | $U_{22}$ | $U_{33}$ | $U_{23}$ | $U_{13}$ | $U_{12}$ |
|---|---|---|---|---|---|---|
| Fe1 | 6.1(2) | 5.2(2) | 6.4(2) | 0.20(19) | –0.02(19) | −0.04(18) |
| K2 | 8.0(5) | 8.1(5) | 7.2(5) | 0 | –0.7(4) | 0 |
| K3 | 10.1(3) | 11.5(4) | 8.6(4) | −0.2(3) | 0.4(3) | −2.7(3) |
| S4 | 6.5(5) | 6.9(5) | 8.4(6) | 0 | −0.9(4) | 0 |
| S5 | 6.0(5) | 9.3(6) | 6.3(6) | 0 | –0.5(5) | 0 |
| S6 | 8.4(4) | 5.6(4) | 7.7(4) | 0.6(3) | 2.0(3) | 0.0(3) |

**Table S3.** Bond lengths for compound **1** (Å)

| Atom | Atom | Length | | Atom | Atom | Length |
|---|---|---|---|---|---|---|
| Fe1 | Fe1 | 2.7760(10) | | K2 | S5 | 3.0886(18) |
| Fe1 | Fe1 | 2.8814(10) | | K2 | S5 | 3.0876(17) |
| Fe1 | K2 | 3.7294(12) | | K2 | S6 | 3.1341(12) |
| Fe1 | K3 | 3.8254(10) | | K2 | S6 | 3.2547(13) |
| Fe1 | K3 | 3.7305(10) | | K3 | K3 | 3.8199(16) |
| Fe1 | K3 | 3.8720(10) | | K3 | K3 | 3.6848(16) |
| Fe1 | K3 | 3.8720(10) | | K3 | S4 | 3.2082(14) |
| Fe1 | S4 | 2.2770(12) | | K3 | S4 | 3.1059(13) |
| Fe1 | S5 | 2.3135(11) | | K3 | S5 | 3.3571(14) |
| Fe1 | S5 | 2.2884(10) | | K3 | S5 | 3.2439(12) |
| Fe1 | S6 | 2.3404(11) | | K2 | K2 | 3.5231(13) |
| | | | | | | |

## 2. Details of powder XRD measurements and Rietveld refinement

*Sample preparation:* The samples were prepared on self-printed sample holders as reported previously.[S1]

*Measurement:* The phase identification, purity, degree of crystallinity, and crystallite size of **1** were investigated using powder X-ray diffraction technique, performed on a *Malvern Panalytical Empyrean* diffractometer equipped with a *PIXcel 1D* detector using Cu-$K_\alpha$ radiation ($\lambda$ = 1.54 Å) at room temperature in reflection mode.

*Rietveld structure refinement:* The PXRD pattern was refined based on Rietveld structure refinement[S7] using *GSAS II*[S8] software. During the refinement, the PXRD diffractogram was refined with the structural parameters regarding background, atomic temperature factor, preferred orientation, zero shift, micro strain, and crystallite size. To reach these aims, in the first step the background is detected based on inverse *Chebyschev* function. After that, the diffractometer type and related parameters are refined based on the *Bragg-Brentano* mode, and finally the PXRD diffractogram is refined according to the crystallographic information file (CIF) of the pure phase of **1** obtained from the single crystal measurement.

For more clarification, the list of main detected reflection in PXRD analysis and the indexes of the corresponding crystal planes are provided in table S4.

**Table S4.** List of the main detected reflections and the indexes of the corresponding crystal planes

| No. | *h* | *k* | *l* | *2Θ (°)* |
|---|---|---|---|---|
| 1 | 1 | 3 | 2 | 14.376 |
| 2 | 2 | 0 | 3 | 15.578 |
| 3 | 0 | 4 | 2 | 16.469 |
| 4 | 3 | 0 | 5 | 24.741 |
| 5 | 2 | 6 | 2 | 26.179 |
| 6 | 2 | 6 | 3 | 27.381 |
| 7 | 2 | 2 | 7 | 28.422 |
| 8 | 1 | 8 | 1 | 30.760 |
| 9 | 1 | 5 | 7 | 35.061 |
| 10 | 5 | 0 | 4 | 35.945 |
| 11 | 3 | 7 | 2 | 42.315 |
| 12 | 2 | 8 | 1 | 44.577 |

### 3. Details of thermal analyses

Thermal analyses including DSC and TG measurements were conducted under nitrogen atmosphere in an alumina crucible, using a STA 449 F3 Jupiter® thermal analyser with a SiC-oven and TG-DSC-sample carrier type S. TGA and DSC measurements were carried out under N2-flow (20mL·min−1) in alumina crucibles. The measurements were carried out on the sample (27.8 mg) by heating in the range of room temperature to 1023 K and then cooling down to the starting temperature, while both heating and cooling rates are 3 K·min$^{-1}$.

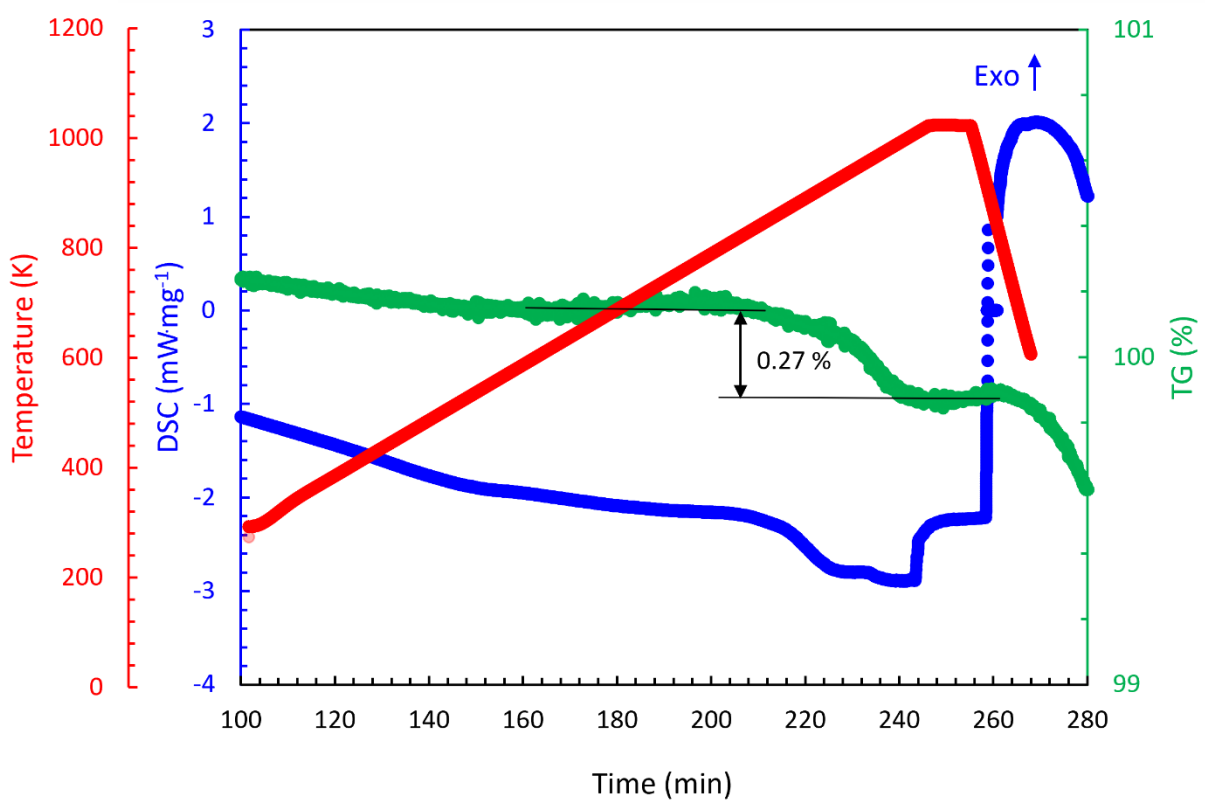


**Figure S1.** DSC profile of **1** (in blue), TG Profile of **1** (in green), and the plot of temperature variation as a function of measurement time (in red). Heating and cooling rates in all measurement are 3 K·min$^{-1}$.

### 4. Details of infrared (IR) spectroscopy

A fine powder of **1** (approx. 50 mg) was placed on the diamond sample holder of the spectrometer inside a glovebox. Infrared spectroscopy measurements were performed using a *Bruker Alpha* ATR-IR-spectrometer.

The IR spectrum (Figure S1) display four main absorption bands in the range of 1015-460 $cm^{-1}$. However, the absorption bands of Fe-S are expected at wavenumbers lower than 400 $cm^{-1}$ which lie outside of the measurement range.[S9]

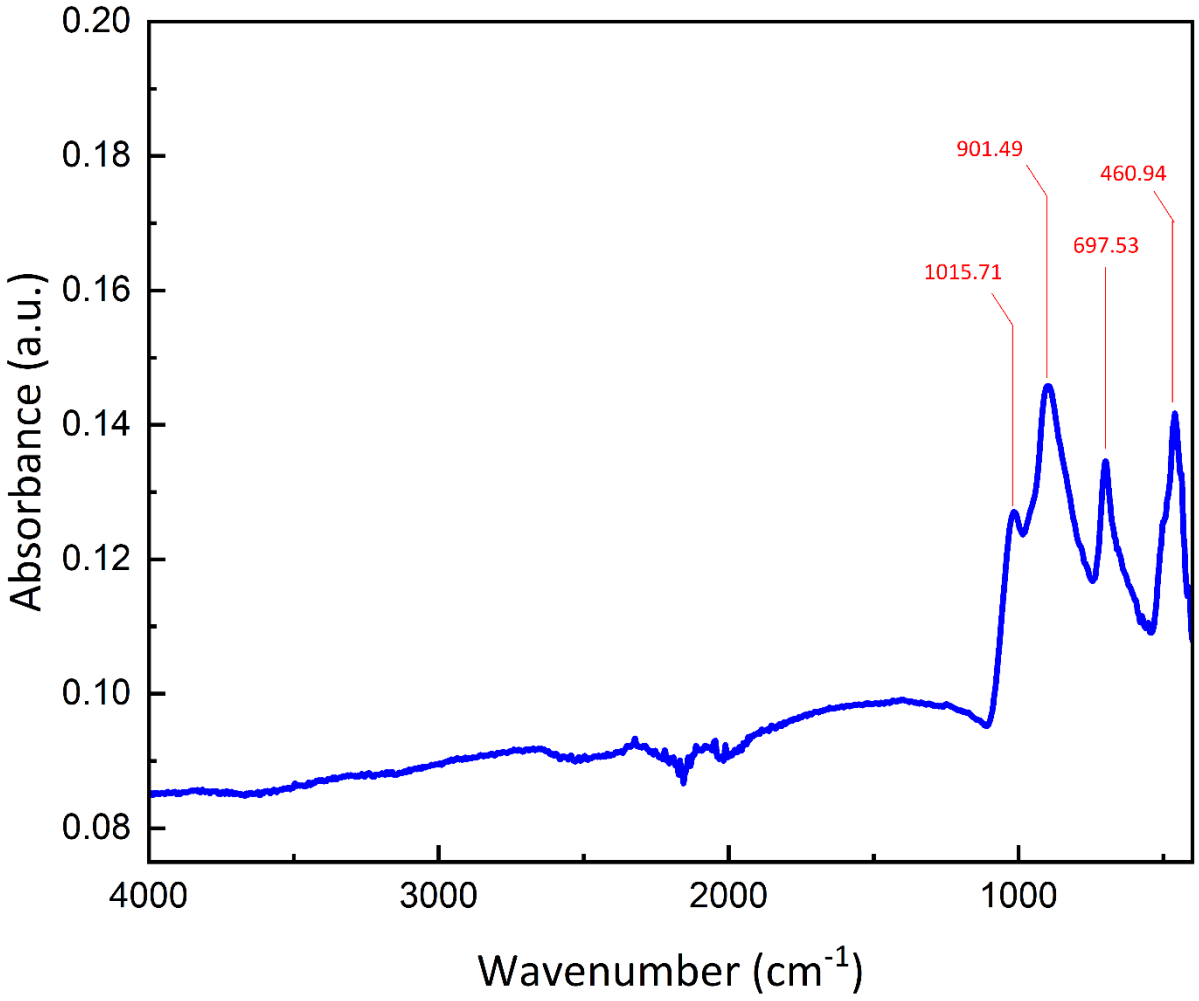


**Figure S2.** Infrared spectrum of **1** measured in the range of 4000-400 $cm^{-1}$.

**5. Magnetic measurements**

*Sample preparation:* Samples of **1** were prepared as a fine powder (approx. 15 mg) in microcapsules of polyethylene.

*Measurement:* The samples were pressed into a brass holder, inserted into the magnetometer, a superconducting quantum interference device (*MPMS-7T* Quantum Design), and measured under a helium atmosphere in the temperature range of 2-400 K. M-H curves were measured at different temperatures under an applied field of 5.00 T. Temperature-scan measurements (FC/ZFC) were done under an applied field of 0.50 T.

The close-up view of the field dependent magnetisation curve (Figure S2) shows a shift in the average point of the coercivities of the curves to the positive field direction (right side), at both temperatures of 3 and 300 K. However, the shift value of the M-H curve at 3 K (2.2 mT) is higher than that of the curve at 300 K (0.7 mT), indicating the existence of a weak exchange bias field at low temperatures.

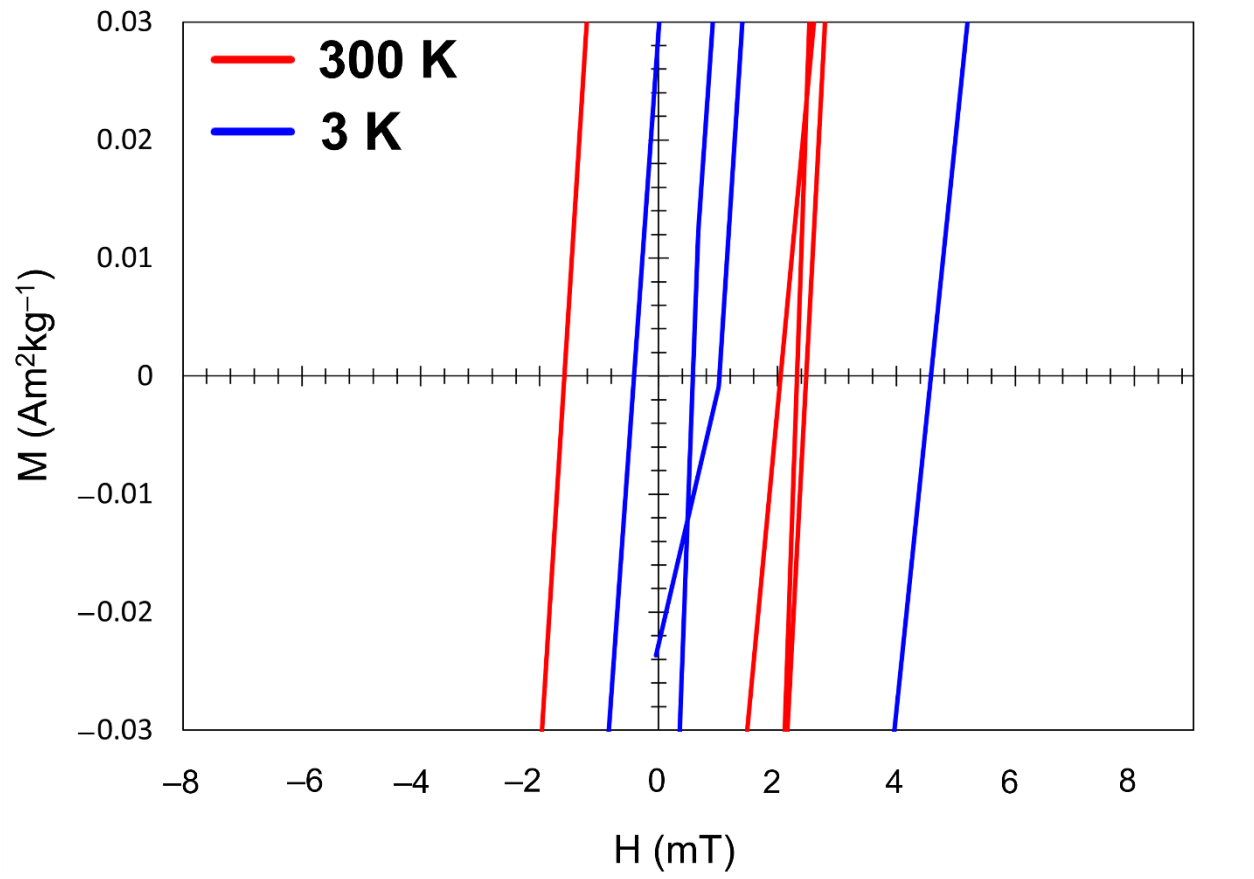


**Figure S3.** Close-up view of the field dependent magnetisation curve as a function of the applied field at 3 and 300 K.

### 6. Dielectric and impedance measurements

*Sample preparation:* To measure electrical properties of the compound, the bulk samples (pellets) were prepared and sintered at appropriate temperatures. Pellets were prepared by filling a cylindrical pressing mould (diameter: 13 mm; height: 38 mm) with a very fine powder of **1** (approx. 400 mg), sealed with electrical tape and parafilm©, and pressed with up to 80 kN·cm$^{-2}$ with a uniaxial hydraulic press under Ar. The pellets were transferred into alumina crucibles inside a silica glass ampoule and sintered at either 723, 823, or 923 K

for 15 h in an electrical tube furnace. After the sintering, the pellet dimensions were 12 mm in diameter and 2 mm in height. Both sides of the pellets of **1** were covered with silver conductive adhesive paste (*abcr*, sheet resistivity $<3.8\times10^{-3}\ \Omega\cdot cm^{-1}$, for a layer thickness of $3.8\times10^{-4}$ cm) as the electrodes and treated at 423 K for 60 minutes in an electrical furnace.

*Measurements:* To calculate the dielectric constant, the main characteristics, such as capacitance *C* and dielectric loss *D* were measured by using a LCR meter (*ET4410, East Tester*). All measurements were carried out at the frequency range of 0.10 to 100 kHz by applying the field of 1 V. The dielectric constant values were calculated based on the following equation.[35]

$$\kappa = C\, d\, \varepsilon_0^{-1} A^{-1} \qquad \text{(S1)}$$

where *C* is the measured capacitance, *A* is the area of the electrode plates, *d* is the distance between the electrodes, and $\varepsilon_0$ is the permittivity of the vacuum ($8.85\times10^{-12}\ m^{-3}kg^{-1}s^4A^2$). Real and imaginary parts of complex impedance, *Z*' and *Z*'', were measured using the electrochemical impedance analyser (EIS, *BioLogic* MTZ-35) at room temperature under 100 mV sine phase at the frequency range of 10 mHz to 1 MHz. For fitting the trend line on the experimental data, the EC-Lab software package (*BioLogic*, V 11.0) was used.

To verify the reliability of the dielectric measurements, a commercial sample of $BaTiO_3$ (BTO, >99%, *abcr*) was prepared as a pellet and investigated according to the reported methods,[S10] which confirmed the reliability of the measuring techniques. [S11-S13]

**7. Details of SEM/EDX measurements**

Finely ground powder of **1** (10 mg) was attached to the surface of measurement stubs using carbon stickers and coated with a carbon film to avoid charge accumulation on the surfaces. Samples were transferred to a *Zeiss Sigma 300VP* field emission scanning electron microscope (FE-SEM), coupled with two *Bruker, Quantax Xflash* 6, 60 $mm^2$, SSD, EDX detectors. For microstructural investigations, SEM imaging was done on the cross section of the sintered pellets using the secondary electron detector. For EDX measurements an optimal working distance of 8.5 mm, a beam aperture of 60 micrometer and a beam energy of 20 kV was used. The *Bruker Esprit* 2.1 software was used to perform standardless EDX measurements and to quantify the data. Point EDX measurements were performed for two different samples at selected locations on the sample as well as EDX maps over an area of the sample.

**8. Details of UV-Visible spectroscopy**

In the range of 200 to 1400 nm, optical absorption was measured on a *Varian Cary 5000* UV/VIS/NIR spectrometer by using a Praying Mantis™ accessory from *Harrick*. The optical band gap of **1** was estimated using Tauc plot by application of the Kubelka-Munk function.[S14]

The optical band gap of the compound was determined using a Tauc plot (Figure S3) calculated from the results of UV-Visible measurements. The shape of the curve indicates the indirect type of the band gap, while the extrapolated intercept with the x-axis (energy values) shows the approx. value of the band gap.

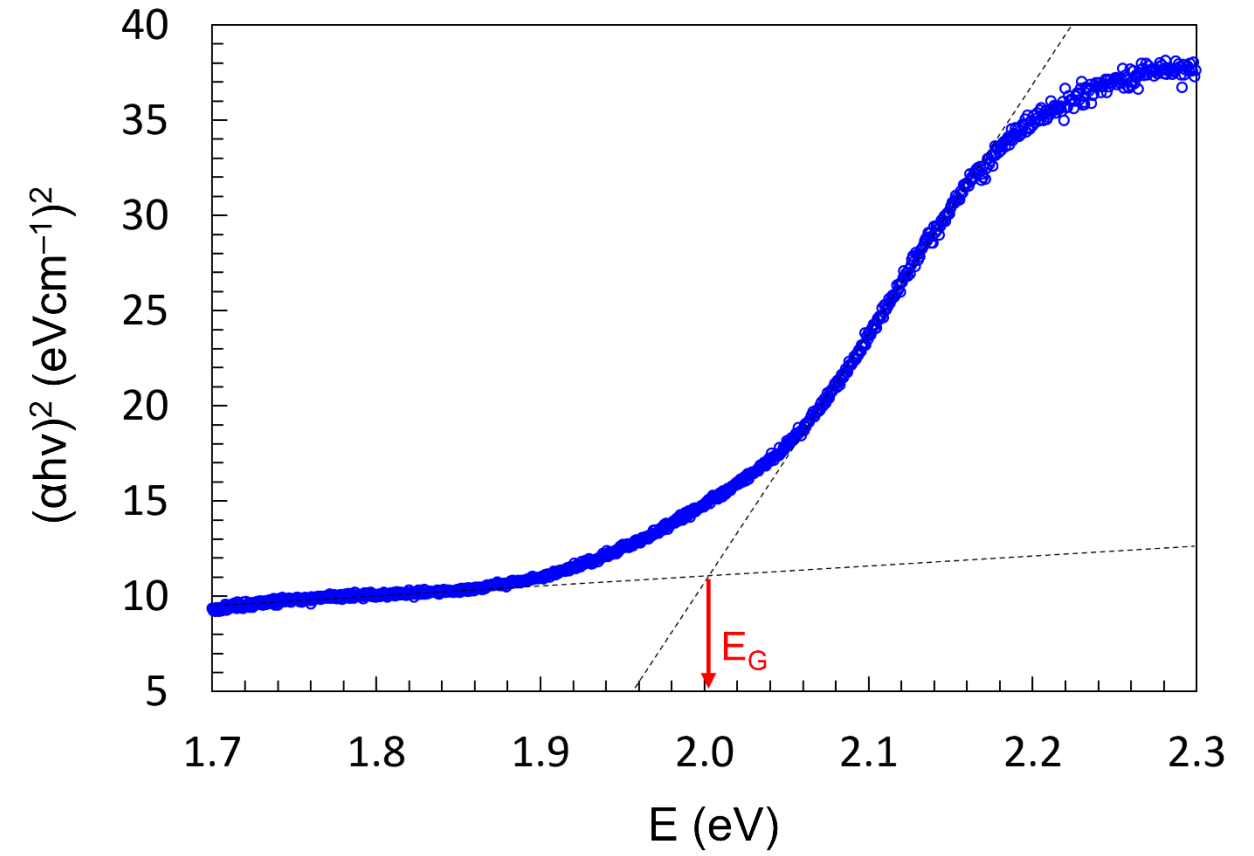


**Figure S4.** Calculated Tauc plot using UV-Visible spectroscopy to determine the indirect optical band gap for compound **1**. The calculated band gap lies around 2.00 eV (red arrow).

**9. Quantum chemical calculations**

Density functional theory (DFT) calculations of the electronic and optical properties were carried out based on the strongly constrained and appropriately normed meta-generalized gradient

approximation (SCAN) functional,[S15] as implemented in the Vienna *ab initio* simulation package (VASP).[S16]

All structures were fully relaxed with a plane-wave basis set cut-off energy of 520 eV until the residual atomic forces were below 0.001 eV·Å$^{-1}$. The Brillouin-zone (BZ) was sampled with a Monkhorst-Pack scheme **k**-grid corresponding to a **k**-spacing of 0.2 Å$^{-1}$ for the relaxations. In order to account for the self-interaction error, an on-site U based on the Hubbard model,[S17-S19] was applied to the Fe orbitals.

A series of DFT+U calculations were carried out with U values 2.0, 2.5, 3.0 and 3.5 eV before selecting a U parameter of 2.5 eV that best described the electronic and magnetic properties of the material. The band structures were plotted along the high-symmetry lines in the BZ and the energies were shifted to align the Fermi level with zero.

The projected electronic band structures of **1**, calculated using quantum chemical calculations, predict an asymmetric band structure for the spin-up and spin-down contributions. The iron ions, particularly Fe-*d* orbitals, have a main role in both spin up and down contributions (Figure S4), as can be determined from the element- and orbital-resolved DOS plots (Figures S5 and S6).

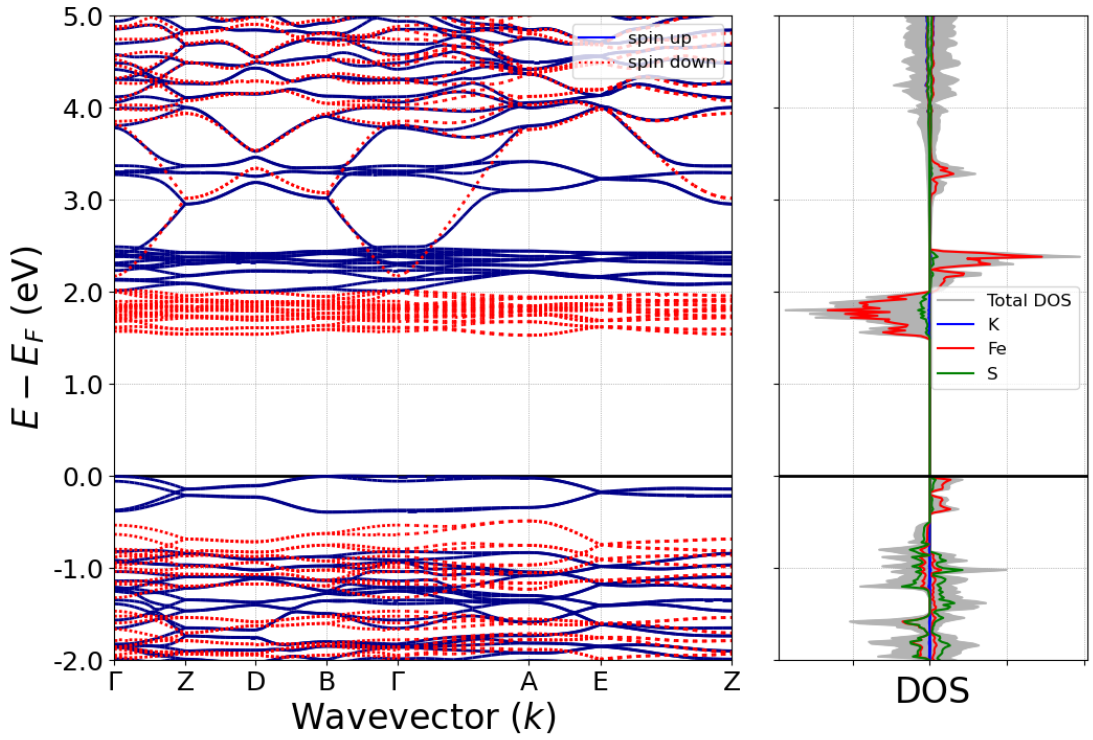


**Figure S5.** Left frame: The electronic band structure of **1** calculated by quantum chemical calculations. Solid lines: Spin up contribution. Dotted lines: Spin-down contribution. The Fermi level is shifted to zero on the energy scale. Right frame: The density of states, DOS, of **1** calculated by quantum chemical calculations.

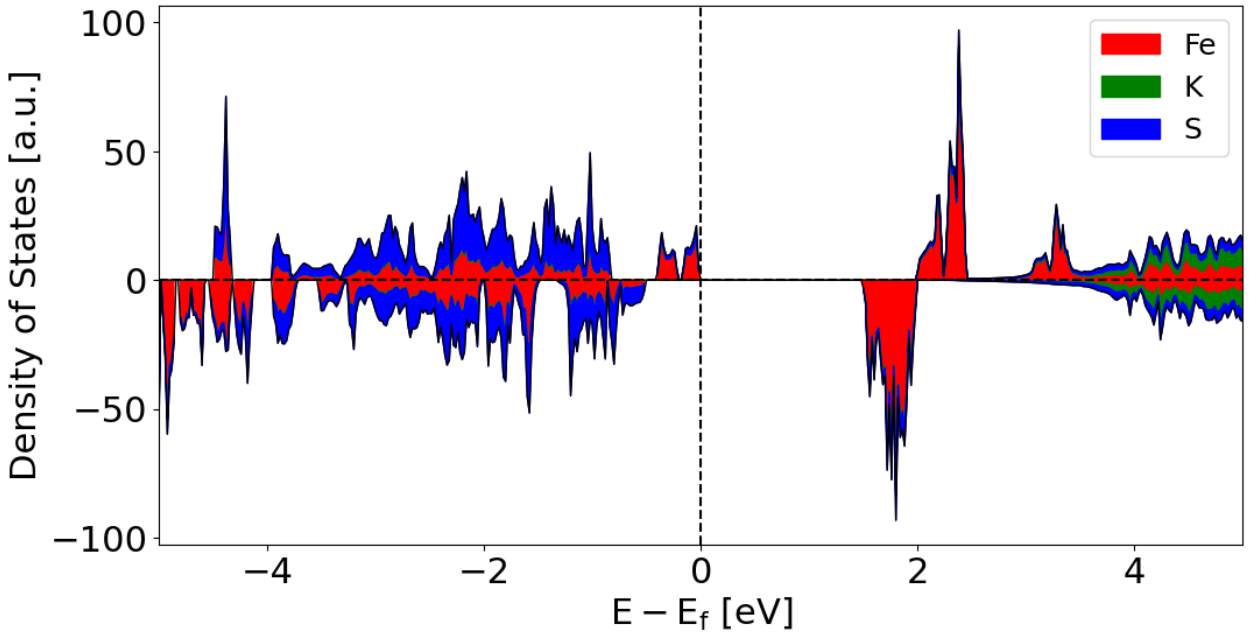


**Figure S6.** The element-resolved density of states of **1** calculated by quantum chemical calculations.

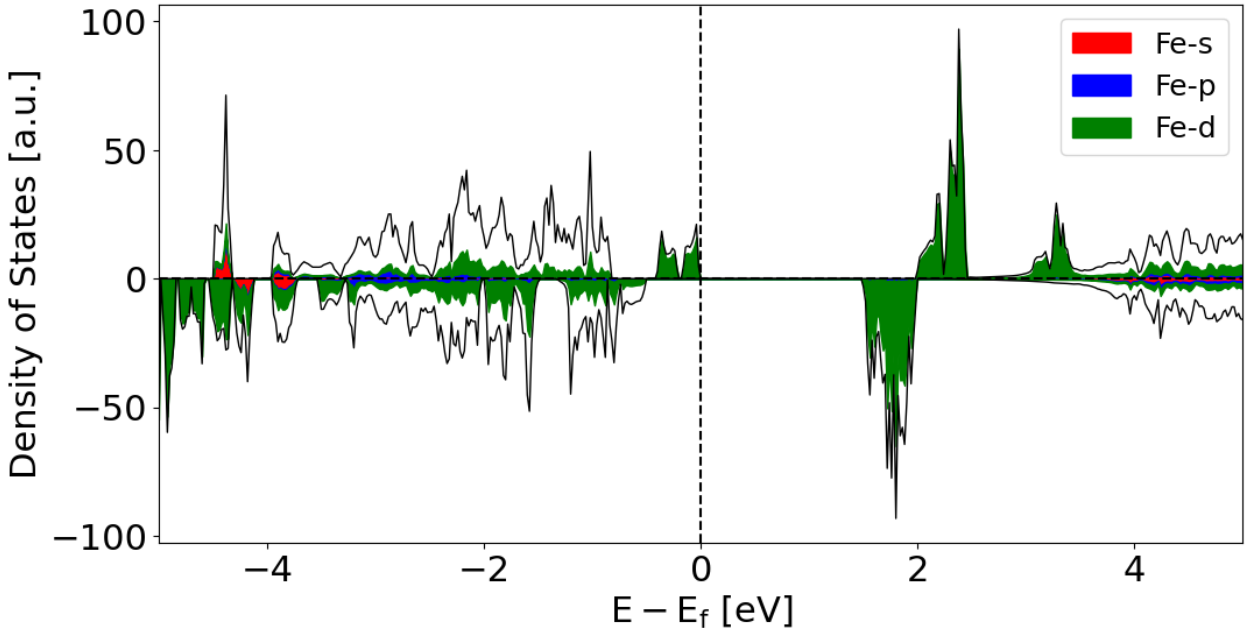


**Figure S7.** The Fe orbital-resolved density of states of **1** calculated by quantum chemical calculations.

## 10. References


S1. F. Fuß, M. Rieckert, S. Steinhauer, M. Liesegang, G. Thiele, 3D-printed equipment to decouple (P)XRD sample preparation and measurement, *J. Appl. Cryst.*, 2022, **55**.

S2. O. V. Dolomanov, L. J. Bourhis, R. J. Gildea, J. A. K. Howard, H. Puschmann, OLEX2: a complete structure solution, refinement and analysis program, *J. Appl. Crystallogr.*, 2009, **42**, 339.

S3. G. M. Sheldrick, SHELXT - Integrated space-group and crystal-structure determination, *Acta Crystallogr. A*, 2015, **71**, 3.

S4. G. M. Sheldrick, Crystal structure refinement with SHELXL, *Acta Crystallogr. C*, 2015, **71**, 3.

S5. K. Brandenburg, DIAMOND (4.6.4), Crystal Impact GbR, Bonn, (**2020)**.

S6. G. M. Sheldrick, SADABS v. 2: Multi-Scan Absorption Correction, Bruker-AXS, WA, **2012**.

S7. a) H. M. Rietveld, Line profiles of neutron powder-diffraction peaks for structure refinement, *Acta. Cryst.*, 1967, **22**, 151; b) H.M. Rietveld, A profile refinement method for nuclear and magnetic structures, *J. Appl. Crystallogr*., 1969, **2**, 65.

S8. B. H. Toby, R. B. von Dreele, GSAS-II: the genesis of a modern open-source all purpose crystallography software package, *J. Appl. Crystallogr.*, 2013, **46**, 544.

S9. Y. Guo, H. Wang, Y. Xiao, S. Vogt, R. K. Thauer, S. Shima, P. I. Volkers, T. B. Rauchfuss, V. Pelmenschikov, D. A. Case, E. E. Alp, W. Sturhahn, Y. Yoda, S. P. Cramer, Characterization of the Fe site in iron−sulfur cluster-free hydrogenase (Hmd) and of a model compound via nuclear resonance vibrational spectroscopy (NRVS), *Inorg. Chem.*, 2008, **47**, 10, 3969.

S10. M. R. Ghazanfari, A. Santhosh, K. Siemensmeyer, F. Fuß, L. Staab, J. C. Vrijmoed, B. Peters, M. Liesegang, S. Dehnen, O. Oeckler, Large exchange bias, high dielectric constant, and outstanding ionic conductivity in single-phase spin glass, *Adv. Electron. Mater.* 2022, 2200483.

S11. W. B. Li, D. Zhou, L. X. Pang, R. Xu, H. H. Guo, Novel barium titanate based capacitors with high energy density and fast discharge performance, *J. Mater. Chem. A*, 2017, **5**, 19607.

S12. N. S. Hari, P. Padmini, T. R. N. Kutty, Complex impedance analyses of n-$BaTiO_3$ ceramics showing positive temperature coefficient of resistance, *J. Mater. Sci.: Mater. Electron.*, 1997, **8**, 15.

S13. L. Khadira, S. Sayouri, A. Elmesbahi, A. Salhi, Investigation of complex impedance and modulus properties of La or/and Ca doped $BaTiO_3$, *Mater. Today: Proc.*, 2019, **13**, 1238.

S14. A. A. Kokhanovsky, Physical interpretation and accuracy of the Kubelka–Munk theory, *J. Phys. D: Appl. Phys.*, 2007, **40**, 2210.

S15. J. Sun, A. Ruzsinszky, J. P. Perdew, Strongly constrained and appropriately normed semilocal density functional, *Phys. Rev. Lett.*, 2015, **115**, 036402.

S16. G. Kresse, J. Furthmüller, Efficient iterative schemes for ab initio total-energy calculations using a plane-wave basis set, *Phys. Rev. B*, 1996, 54, 11169.

S17. A. Rohrbach, J. Hafner, G. Kresse, Electronic correlation effects in transition-metal sulfides, *J. Phys.: Condens. Matter*., 2003, **15**, 979.

S18. A. I. Liechtenstein, V. I. Anisimov, J. Zaanen, Density-functional theory and strong interactions: Orbital ordering in Mott-Hubbard insulators, *Phys. Rev. B* 1995, **52**, R5467.

S19. S. L. Dudarev, G. A. Botton, S. Y. Savrasov, C. J. Humphreys, A. P. Sutton, Electron-energy-loss spectra and the structural stability of nickel oxide: An LSDA+U study, *Phys. Rev. B* 1998, **57**, 1505.